analytical chemistry

pubs.acs.org/ac Article

Diffusion Mapping with Diffractive Optical Elements for Periodically Patterned Photobleaching

Dustin M. Harmon, Ziyi Cao, Alex M. Sherman, Nita Takanti, Kevin Murati, Maura M. Wimsatt, Michelle L. Cousineau, Yechan Hwang, Lynne S. Taylor, and Garth J. Simpson*

Cite This: *Anal. Chem.* 2024, 96, 10161−10169 Read Online

ACCESS | Metrics & More | Article Recommendations | Supporting Information

ABSTRACT: Fourier transform-fluorescence recovery after photobleaching (FT-FRAP) using a diffractive optical element (DOE) is shown to support distance-dependent diffusion analysis in biologically relevant media. Integration of DOEs enables patterning of a dot array for parallel acquisition of point-bleach FRAP measurements at multiple locations across the field of view. In homogeneous media, the spatial harmonics of the dot array analyzed in the spatial Fourier transform domain yield diffusion recovery curves evaluated over specific well-defined distances. Relative distances for diffusive recovery in the spatial Fourier transform domain are directly connected to the 2D (h,k) Miller indices of the corresponding lattice lines. The distribution of the photobleach power across the entire field of view using a multidot array pattern greatly increases the overall signal power in the spatial FT-domain for signal-to-noise improvements. Derivations are presented for the mathematical underpinnings of FT-FRAP performed with 2D periodicity in the photobleach patterns. Retrofitting of FT-FRAP into instrumentation for high-throughput FRAP analysis (Formulatrix) supports automated analysis of robotically prepared 96-well plates for precise quantification of molecular mobility. Figures of merit are evaluated for FT-FRAP in analysis for both slow diffusion of fluorescent dyes in glassy polymer matrices spanning several days and model proteins and monoclonal antibodies within aqueous solutions recovering in matters of seconds.

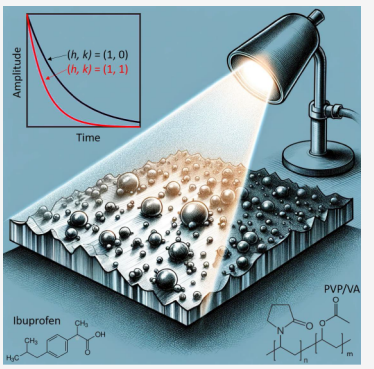

INTRODUCTION

FRAP is a technique commonly used for the characterization of mobility in various disciplines, such as early-stage rejection of monoclonal antibody (mAb) candidates likely to exhibit low bioavailability upon subcutaneous injection.[1,2] Molecular mobility in FRAP is assessed by photobleaching a fluorescent sample with a conventionally Gaussian beam profile using a high-powered beam of light. For mobile samples, photobleached molecules will diffuse out of the bleach spot, while nonphotobleached fluorescent molecules diffuse into the bleach spot, allowing the recovery of fluorescence over time from diffusive motion. With knowledge of the initial bleach shape, the fluorescent recovery can be fit to a mathematical model, allowing for quantification of the diffusivity of fluorescently labeled analyte.[3] FRAP was first performed by Peters et al. in 1974 to measure the diffusion of proteins in the membranes of red blood cell ghosts.[4] In studies more closely aligned with assessing subcutaneous mobility in an *in vitro* assay, FRAP has been used to study protein aggregates,[5] diffusivity in microporous tissue engineering scaffolds,[6] diffusion anisotropy in porcine ligaments,[7] and membrane protein mobility in lipidic mesophases.[8] Furthermore, FRAP has been used in the study of pharmaceutical materials to quantify molecular transport in hydrogels,[9−14] and extracellular matrices to improve drug delivery methods.[15,16]

Despite its broad applicability, conventional point-bleach FRAP has several limitations. FRAP requires the molecule of interest to fluoresce through the use of a fluorescent label, native autofluorescence, or through the addition of a local fluorescent reporter. Labels are often bound to charge-carrying functional groups, such that fluorescent labeling could impact both long-range electrostatic interactions and short-range local interactions.[17] Consequently, the mobility of the labeled protein target may not be representative of the mobility of the unlabeled protein of interest. Additionally, FRAP measurements often require precise knowledge of the photobleaching profile for an accurate assessment of diffusion. However, high laser power used for improved signal-to-noise enhancement can cause bleaching saturation, affecting the overall photobleaching profile, and can skew calculated values of the diffusion coefficient by over an order of magnitude.[18] Moreover, spatial heterogeneity in molecular mobility can routinely arise within structured samples (e.g., biological microscopy), which can bias results from FRAP measurements

Received: December 15, 2023
Revised: May 10, 2024
Accepted: May 15, 2024
Published: June 12, 2024

acquired at discrete locations. As conventional FRAP measurements are most routinely performed by photobleaching a tightly localized spot for high bleach depth and fast recovery times to minimize $1/f$ noise, the small region of the sample probed by point-bleach FRAP may not be representative of the overall diffusion characteristics of a heterogeneous or structured sample.[19,20] Lastly, anomalous diffusion can be challenging to quantitatively and definitively discriminate from normal diffusion in point-bleaching FRAP measurements.[19]

Fourier transform (FT)-FRAP was shown to address many of the limitations cited above for conventional point-bleach FRAP.[21,22] In FT-FRAP, a fluorescent sample is photobleached using periodically patterned illumination, with the subsequent recovery analyzed in the spatial-FT domain. For the analysis of homogeneous samples by FT-FRAP, distributing the bleach power throughout the field of view (FoV) minimizes contributions from spatial heterogeneity.[21−23] Distribution of the photobleach over a larger region of the FoV also allowes for a larger integrated photobleaching power, with corresponding increases in the overall signal-to-noise ratio (SNR) in the spatial frequency domain. Moreover, simultaneous analysis of multiple harmonics in the spatial frequency domain enables diffusion characterization at several discrete length scales. Such analysis was shown to be highly sensitive to departures from normal diffusive motion.[22]

In more recent work on spatially heterogeneous assemblies, FT-FRAP coupled with image segmentation was shown to support quantification of molecular mobility within several domains in a single FoV simultaneously. Here, a periodic "comb" of equidistant coparallel lines was used as the photobleach pattern. Analysis of the bleaching profile in Fourier space was shown to allow high signal-to-noise recovery of the diffusion coefficient for both normal and anomalous diffusion.[21,22] For heterogeneous samples, image segmentation enabled isolated Fourier-domain analysis within regions of arbitrary shape. Recombining segmentation results allowed the generation of spatially resolved diffusion maps in phase-separated model amorphous solid dispersion thin films.[22,23]

While FT-FRAP allows for the removal of many of the limitations found in conventional FRAP measurements, the beam-scanning approach used in previous implementations of FT-FRAP has some important limitations. Although compatible with laser scanning confocal fluorescence microscopy instrumentation and multi-photon excitation, the beam-scanning architecture used previously is not trivially compatible with more commonplace instrumentation based on focal plane array detectors. Furthermore, since the system is restricted to periodic line bleaching, diffusion is only probed in the direction perpendicular to the comb "teeth". Thus, the analysis of anisotropic samples described by a diffusion tensor (i.e., samples in which diffusion in certain directions is distinct) will only report on the component of diffusion orthogonal to the comb axis with this architecture. Finally, resonant mirrors for the fast-scan axis in the previous comb-bleach work supported efficient heat dissipation for multiphoton excitation but could produce drift in amplitude and phase, complicating precise image registry across a time series. As such, fine features or small domains are challenging to analyze using beam-scanning comb-bleach FT-FRAP, particularly over extended timeframes.

In this work, the theoretical foundation for and experimental implementation of FT-FRAP with 2D periodicity is presented and applied for analysis of diffusivity in proteins and small molecules, capable of recovering diffusion coefficients within highly localized features in domains of arbitrary shape. Briefly, a high-throughput FRAP instrument with autoencoded sample positioning was retrofitted with a diffractive optical element (DOE) supporting 2D periodically structured illumination. Power distribution across the entire field of view using a "dot-array" pattern enabled substantial increases in the integrated photobleach power, concentrated into a small number of bright puncta in the spatial Fourier transform domain. Further, the intrinsic periodicity within the original 2D- patterned illumination defined a well-characterized distance dependence for all harmonics investigated. Differences in recovery times for different peaks in the spatial FT domain can be interpreted theoretically in terms of Miller indices commonly used in diffraction descriptions.[24] Periodically patterned illumination yielded quantitative improvements in high throughput measurements of protein mobility in viscous aqueous solutions and small molecule mobility in glassy-polymer matrices relative to conventional point-bleach FRAP analyses. Performing the diffusion analysis in the spatial frequency domain following this patterned illumination allowed for: (i) increased SNR in measurements, (ii) reduced bias from spatially varying sample heterogeneity, (iii) simplified mathematical modeling by removing uncertainties related to the point-spread function, and (iv) single-shot recovery of diffusion at several length scales to precisely determine the presence or absence of anomalous diffusion within heterogeneous media.

Theoretical Foundation. The core theoretical foundations of FRAP with periodically patterned illumination with Fourier-domain analysis have been detailed previously for beam-scanning comb-bleach FT-FRAP,[21−23] forming the foundation for the extension herein to dot-array illumination using focal plane array detection. In the case of isotropic diffusion, Ficks Law results in a simple analytical form for the concentration-dependent recovery in the spatial Fourier transform domain. The two-dimensional solution in this limit is given by eq 1, in which $\tilde{C}$ is the spatial FT of the concentration profile, $\overline{\nu}_x, \overline{\nu}_y$ are the spatial frequencies in the x and y directions, respectively, t is time, and D is the isotropic diffusion coefficient.

$$\tilde{C}(\overline{\nu}_x, \overline{\nu}_y, t) = \tilde{C}(\overline{\nu}_x, \overline{\nu}_y, 0)\, e^{-(2\pi)^2(\overline{\nu}_x^2+\overline{\nu}_y^2)Dt} \quad (1)$$

In the spatial frequency domain, the dot-array pattern with a square lattice constant of x^0 transforms to another dot array of harmonic frequencies with a square lattice constant of $\overline{\nu}^0 = 1/x^0$, as shown in Figure 1D. This optical approach in 2D shares qualitative similarities with X-ray and electron

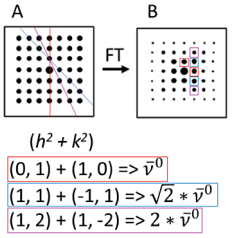

Figure 1. Schematic depicting photobleaching patterns with a dot array in real space (A), which Fourier transforms to a two-dimensional set of equally spaced puncta (B). Each harmonic ($h^2 + k^2$) corresponds to diffusion at a discrete length scale.

https://doi.org/10.1021/acs.analchem.3c05728
Anal. Chem. 2024, 96, 10161−10169

diffraction, in which puncta in the FT-domain (i.e., "*k*-space") correspond to harmonics of the inverse lattice constants. As such, we can leverage the established Miller index nomenclature from diffraction theory[24] to describe FT-FRAP with dot-array illumination. Specifically, the primitive square 2D lattice used in this work with a lattice constant of a^0 ($=b^0$) will produce puncta in the FT domain corresponding to periodic lattice lines within the array. For example, the Miller indices for the set of horizontal lines intersecting the puncta along the *x*-axis produce an (h,k) Miller index of (0,1), corresponding to the punctum in the FT domain at position $\overline{\nu}_x, \overline{\nu}_y(0, \overline{\nu}^0)$. Higher-order reflections corresponding to larger Miller indices inform over shorter distances relative to the lattice constant, such that the punctum at index (0,2) probes recovery over length scales of $a^0/2$ and the punctum at (1,2) recovery over lengths of $a^0/\sqrt{1^2 + 2^2} = a^0/\sqrt{5}$, etc. The time-dependent decay of a given punctum for isotropic diffusion in 2D is directly related to its corresponding set of 2D Miller indices (h,k).

$$\tilde{C}_{(h,k)}(\overline{\nu}, t) = \tilde{C}(h\overline{\nu}_x^0, k\overline{\nu}_y^0, 0)\, e^{-(2\pi\overline{\nu}^0)^2(h^2+k^2)Dt} \quad (2)$$

All results presented herein are for studies of molecular diffusivity within thin spin-cast films, such that 3D diffusion along the optical axis can be neglected, consistent with the two-dimensional model given in eq 2. In addition, for the samples interrogated in this study, normal, isotropic diffusion is expected, with peak intensities from analogous reflections pooled together to calculate the diffusion coefficient with a higher statistical confidence.

Holographic Pattern Selection. Several considerations informed the selection of the dot-array patterns used for FT-FRAP analysis, which included both a 21 × 21 dot array and a 50 × 50 dot array pattern. First and foremost was the range of diffusion recovery times anticipated over the distances defined by the periodicity of the array. Derivations for estimation of the maximum and minimum diffusion coefficients (D_{max} and D_{min}, respectively) are detailed in the Supporting Information, resulting in the following expressions: $D_{max} \cong (\text{fps}\cdot W^2)/(4\pi^2 N^2)$, $D_{min} \cong \text{FWHM}^2/(\pi^2 t_{max})$, in which fps is the frames per second of the camera, W is the width of the image in pixels, $N \times N$ is the dot-array dimension, FWHM is the full width and half-maximum of the photobleach point spread function, and t_{max} is the maximum measurement time. The range of diffusion coefficients accessible for the 21 × 21 was calculated to be ~110 $\mu m^2/s < D <$ ~2.5 × 10^{-4} $\mu m^2/s$. In practice, the maximum temporal resolution is limited by the frame rate of the camera and the signal to noise achievable at high frame rates.

Materials and Methods. PVPVA (Kollidon VA 64) was supplied by the BASF Corporation (Ludwigshafen, Germany). Rhodamine 6G (R6G) was purchased from Sigma-Aldrich (St. Louis, MO). Goat anti-mouse IgG (H+L) Secondary antibody, rhodamine, was purchased from Invitrogen (Rockford, IL). Pierce protein-free T20 phosphate buffered saline (PBS) blocking buffer was purchased from Thermo Scientific (Rockford, IL). Sodium hyaluronate (1.0−1.8 MDa) was supplied by Lifecore Biomedical (Chaska, MN). Glycerol was purchased from Sigma-Aldrich (St. Louis, MO). Ibuprofen was purchased from ThermoFisher Scientific (Waltham, MA).

Thin films were prepared by spin coating using a KW-4A spin coater (Chemat Scientific, Northridge, CA). Stock solutions of PVPVA and R6G were prepared in methanol with a 10% w/v solid content. An aliquot of stock solution (100 μL) was placed on a cover glass (#1.5 thickness) and spin coated at 1000 rpm for 10 s, followed by 3000 rpm for 45 s. They were then dried in a vacuum oven overnight before performing measurements. To conduct FT-FTAP analysis, the dried film sample was first transferred into a controlled environment for *in situ* stability testing (CEiST) system, described in detail by Sarkar et al.[25] Relative humidity of 97% and ambient temperature of 25 ± 1 °C were maintained for all experiments through shared headspace with a vapor equilibrated with saturated potassium sulfate aqueous solution.

High-throughput sample plates were prepared using a Mosquito nanoliter liquid handling system (sptlabtech) for drop-setting protein and matrix solutions onto Laminex UV Plastic Base 100 Micron (Molecular Dimensions) 96-well plates before being covered with a Laminex Film Cover (Molecular Dimensions). Two plate preparations were used: (i) a constant viscosity plate was robotically prepared with 300 nL of IgG solution in 50/50 PBS/glycerol (0.7 mg/mL IgG) followed by 300 nL of 50/50 PBS/glycerol to a total well volume of 600 nL, and (ii) a varying viscosity plate was prepared with 300 nL of IgG solution in 50/50 PBS/glycerol, followed by the addition of PBS or PBS/glycerol mixture for tuning viscosity across the plate. Final glycerol volume percentages are as follows: column 1−2−25% glycerol, column 3−4−33% glycerol, column 5−6 and 11−12−50% glycerol, column 7−8−58% glycerol, and column 9−10−63% glycerol.

Ibuprofen−PVPVA samples were prepared with 15% ibuprofen wt % and 0.1% Nile Red fluorescent reporter. The ibuprofen−PVPVA thin films were spin coated using the same parameters previously mentioned for the PVPVA thin films. For imaging, the CEiST system was set to 37 °C, and relative humidity was maintained at 97%.

Dot-Array FRAP. A commercial high-throughput FRAP microscope (Formulatrix, Bedford, MA) was modified in-house to support periodically patterned illumination during photobleaching for FT-FRAP experiments, as shown in Figure 2. A detailed description of the commercial microscope prior to modification has been published previously.[26] To perform

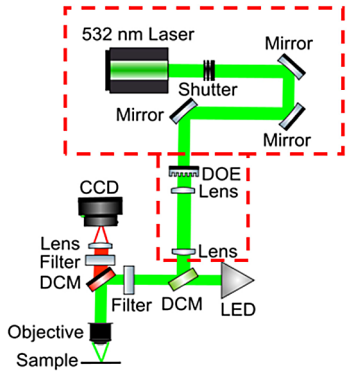

Figure 2. Instrument schematic of the FRAP system modified for FT-FRAP analysis. A DOE produced a dot-array photobleach pattern, and a 4f relay lens pair provided beam expansion and reduced the angle-spread of the dot-array pattern at the back of the objective. A narrow-band DCM was used to combine the 532 nm green beam with the broader-band light provided by a green LED. Fluorescence was detected in transmission through a second (leftmost) DCM using a focal plane array CCD detector. DCM = dichroic mirror, DOE = diffractive optical element, CCD = charge-coupled device camera, LED = broadband green light-emitting diode.

https://doi.org/10.1021/acs.analchem.3c05728
Anal. Chem. 2024, 96, 10161−10169

dot-array FT-FRAP, a diffractive optical element (DOE) [Holoeye Photonics AG, p/n DE-R 389 (21 × 21) or DE-R 388 (51 × 51)] was added to the photobleach light path of the instrument. A 4x beam expansion using a 4*f* relay lens pair [Thorlabs, LA1027-A (*f* = 35 mm, A coated, planoconvex) and Thorlabs, LA1986-A (*f* = 125 mm, A coated, planoconvex)] served to both improve the tightness of focus by matching the beam diameter to the entrance pupil of the objective and (more importantly) reduce the angle spread of the dot-array pattern to within the acceptance angle of the objective. To compensate for the distribution of power across many focal points, a 4 mW, 532 nm photobleaching laser (*Z*-laser) used for point-bleach FRAP measurements in the commercial instrument was replaced with a 5 W maximum 532 nm continuous-wave laser (Millenia V), using software controls for laser power adjustment. The photobleach time was approximately 1 s and produced a dot-array pattern that could be analyzed in the spatial frequency domain for diffusion characterization. Postbleach images were then collected using a focal plane array detector illuminated by a green LED light source. Photobleach powers of 12 mW (30s exposure) were measured at the sample plane for the PVPVA−R6G samples, while 200 mW photo-bleach power was used for the IgG samples and Ibuprofen−PVPVA samples (1 s exposure). Under these conditions, no laser-induced perturbations in the fluorescence intensity were detectable that might indicate a significant local temperature change upon photobleaching. Fluorescence is a sensitive local probe for transient temperature changes, with the quantum efficiency changing by ∼1/°C for many common fluorophores.[27]

Data Analysis. Images from FT-FRAP experiments were analyzed using custom image processing software written in-house in MATLAB. For the FT-FRAP with DOE analysis, image stacks were first cropped to square images centered about the "zero-order" undiffracted photobleach spot (corresponding to the undiffracted light passing through the DOE). The image stack was then converted to the spatial frequency domain using the two-dimensional fast FT function. At each time point, the integrated magnitudes of the accessible lattice peaks were determined following baseline subtraction. The time-dependent decays in magnitude for given reflections (or combinations of reflections) were fit to single exponential decays to recover maximum likelihood estimates for the parameter *D* according to eq 2. Uncertainties in each a_n parameter of the fit for FT-FRAP were obtained from the standard error of the fits σ_{fit} and the variance/covariance matrix $\boldsymbol{\alpha}$ calculated from the Jacobian $\mathbf{J}$ by $\boldsymbol{\alpha} = \mathbf{J}^{\mathrm{T}}\mathbf{J}$.

For high-throughput analysis, outlier rejection criteria were established to reject samples if: 1) the initial Gaussian point-bleach width was greater than 30 pixels or narrower than 8 pixels, indicative of inaccurate autofocusing; 2) the asymptotic first harmonic recovery of less than 75% or greater than 125%, indicating recovery unexpected for this set of samples; 3) the uncertainty in the recovered parameter was greater than 33% of the parameter; 4) a negative-valued diffusion coefficient was recovered; or 5) the camera exhibited saturation or low signal at the center of the prebleach image.

For comparison with conventional point-bleach FRAP, the zero-order photobleach was fit at each time point in a given recovery to yield the Gaussian width σ_b^2 and amplitude $A(t)$. The decay in amplitude was subsequently fit to eq 3 to recover the maximum likelihood estimate (MLE) of the diffusion coefficient *D* and the mobile fraction *F*.

$$A(t) = \frac{(A_0 - F)\sigma_b^2}{\sigma_b^2 + 2Dt} + F \tag{3}$$

Simulations. Diffusive recovery was modeled by iterative convolution with a preset 2D digital filter described previously.[23] All image operations were performed exclusively in the real-space domain. The initial prerecovery images designed to replicate the loss in intensity immediately following instantaneous photobleaching were generated by convolution of a single-pixel (infinitely sharp) dot-array bleach pattern with a Gaussian point-spread function to simulate the photobleach illumination. A representative real-space simulation is shown in Figure 3A, consisting of a periodic series of narrow puncta of reduced concentrations of fluorescent molecules. The dot-array pattern was intentionally rotated ∼15 to minimize overlap with horizontal and vertical features in the spatial frequency domain associated with the rectangular nature of digital images. Prior to Fourier transformation, postbleach images were normalized by the average prebleach image before cropping to avoid edge and vignetting effects.

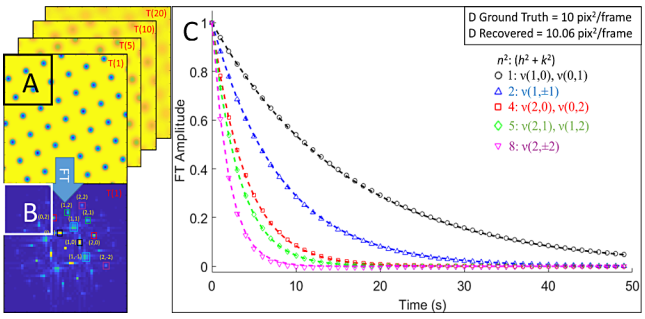

Figure 3. Simulated results for dot array photobleach and recovery of homogeneous normal diffusion. The real-space recovery image stack is shown in panel A, with $T(1)$ corresponding to the first postbleach image. The spatial-FT of first postbleach image [A] is shown in panel B, with corresponding puncta labeled with their Miller indices. Recovery curves for harmonics (1, 0) through (2, 2) are shown in panel C, where the set of curves is fit to a single global parameter for recovering diffusion. The global results of all harmonics to recover the most probable normal diffusion coefficient are given by the dashed curves.

RESULTS AND DISCUSSION

Simulations. The proposed approach for structured illumination with a dot-array photobleach pattern was first evaluated in simulations with known ground-truth diffusivities. Spatial FT following periodically patterned photobleaching yielded another dot-array pattern in the spatial frequency domain. Theory predicts that the decay in amplitude is dependent on both *D* and the (h, k) Miller index of the peak, according to eq 2. The higher spatial frequencies with increasing $(h^2 + k^2)$ in *k*-space correspond to recovery over shorter distances in real space. Peaks with identical values of $n^2 = h^2 + k^2$ are expected to measure diffusion along the same interval of distance. Thus, analogous peaks are color coated in Figure 3C (e.g., the peaks highlighted in black each represent the lowest frequency spacing of the dot-array bleach pattern in orthogonal directions and measure diffusion along the greatest distance interval). For homogeneous samples that are expected to contain only isotropic diffusion, peak intensities from analogous harmonics were pooled together to calculate decays

https://doi.org/10.1021/acs.analchem.3c05728
Anal. Chem. 2024, 96, 10161−10169

from eq 2. Simulated results for a noise-free dot matrix bleach and recovery are shown in Figure 3. A global fit to the normal diffusion parameter D of the first 5 harmonic decays [(1,0) through (2,2)] is shown in Figure 3C. For a ground truth input of 10 pix^2/frame, the diffusion value recovered was 10.06 pix^2/s frame, supporting the validity of the analysis approach in simulations designed to replicate key critical features of the experiments.

Experimental Studies of Isotropic Media. Results for the FT-FRAP analysis of R6G in PVPVA are shown in Figure SI3. As a complement to the studies in relatively viscous polymeric thin film materials, patterned photobleaching using the dot-array pattern was also performed on R6G-labeled goat antimouse immunoglobulin G (IgG) in PBS/glycerol (50/50 vol %). Figure 4 shows a representative FT-FRAP experiment

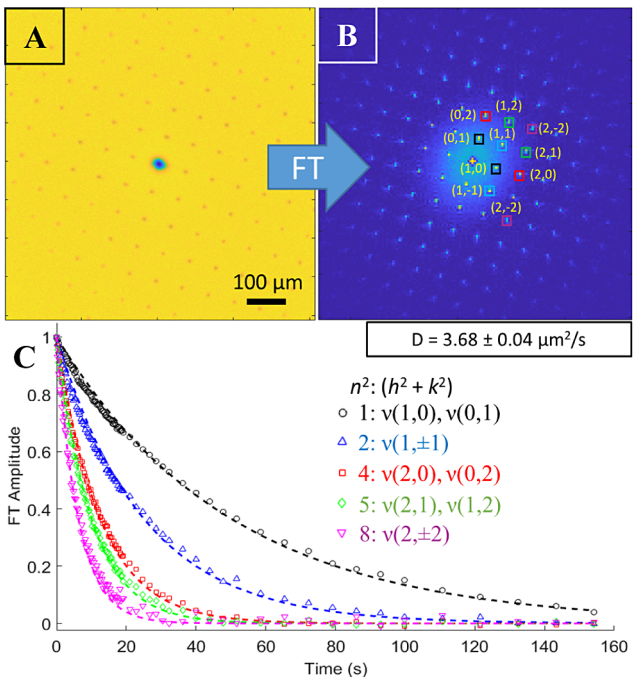

Figure 4. Representative measurements are shown for a high-throughput experiment of IgG in 50/50 PBS/glycerol from a constant-viscosity 96-well plate. Panel A contains the first image after photobleaching, normalized by an average of 3 prebleach images, the spatial FT of which is shown in panel B. In panel C, time-dependent recovery curves are shown for harmonics (1, 0) through (2, 2), along with a maximum likelihood global fit of all harmonics (dashed curves) to recover the most probable diffusion coefficient for normal diffusion.

and the recovered diffusivity. Overall, the recovery curves are collectively in excellent agreement with normal diffusion, with relative decay rates described by the corresponding set of Miller indices. For the 600 nL samples with constant viscosity robotically prepared on 96-well plates, the average diffusion coefficient from FT-FRAP analysis was D = 4.0 ± 0.7 μm^2/s from 276 replicates.

The sample-to-sample RSD for the R6G-IgG was 17%, compared to the RSD from the fits of 1.4%. Based on this substantial disparity between measurement and replicate RSD, we attribute the uncertainty in the recovered values from multiple replicates to variability in sample preparation. For the aqueous glycerol solutions, small differences in volumes dispensed by the liquid-handling robot can lead to large relative uncertainties within droplets of only 600 nL nominal volume. For comparison, the zero-order photobleach spot was analyzed separately. The average diffusion coefficient recovered by point-bleach analysis of the zero-order diffraction peak according to fits to eq 3 yielded a diffusion coefficient of 4.9 ± 0.7 μm^2/s.

The measurements shown in Figure 4 for aqueous solutions were well-fit to the same 2D diffusion model used for thin films. However, diffusion is not constrained to just two dimensions in aqueous media. In our experimental design, excitation was intentionally performed using a "pencil beam" at the focus, in which the excitation beam underfilled the back aperture of the objective to throttle the effective numerical aperture. As a consequence, the excitation profile produced a Rayleigh length along the optical axis approximately 10- to 100-fold greater than the cross-sectional beam waist in the focal plane. Under these conditions, one can reasonably model the 3D photobleaching pattern as an extended "bed of nails", in which diffusion along the optical axis can be safely neglected. This expectation is consistent with the experimental results shown in Figure 4 for recoveries in water/glycerol solutions, for which axial diffusion is anticipated to contribute to a greater extent than in the thin spin-cast films. The presence of significant axial diffusion would manifest as a recovery impacting the amplitude but not the shape of the photobleach spots, producing an identical time-dependent recovery at all spatial harmonics within the (x,y) plane. As shown previously in thin films,[23] such deviations from expectations for normal 2D diffusion are readily quantifiable in FT-FRAP but below the limit of detection in these studies of water/glycerol solutions. The observation of trends consistent with normal 2D diffusion across nearly 2 orders of magnitude in recovery times shown in Figure 4 is in good agreement with pencil-beam illumination and 2D diffusion kinetics.

Interestingly, all of the samples investigated herein were clearly consistent with normal diffusion. As demonstrated in prior work,[22] FT-FRAP is remarkably sensitive to subtle departures from normal diffusion through comparisons of the recovery times measured for different spatial harmonics. Distance-dependent diffusivity from Levy flight and variances in local dwell times can both be modeled using the Mittag-Leffler equation with fractional exponential decays. In FT-FRAP, these subtle departures from normal diffusion are readily apparent from comparisons of the decay rates for the different spatial frequencies as departures from the anticipated (h^2+k^2) scaling anticipated for normal diffusion.

Similar trends were observed for the 96-well plate prepared with varying concentrations of glycerol for a gradient in viscosity across the plate. Recovered diffusivities are shown in Figure 5. A clear trend with viscosity is observed across the plate; the average diffusion of IgG in 25% glycerol/PBS was shown to be 13 ± 2 μm^2/s, transitioning to 2.6 ± 0.4 μm^2/s in 63% glycerol. Consistent with expectations, increases in the glycerol volume fraction resulted in higher viscosity and slower diffusion. Recovered coefficients from point-bleach analysis and FT analysis are compared in Figure 5. The Stokes–Einstein equation provides a simple predictive framework for modeling the theoretical diffusivity of a molecule of hydrodynamic radius (R_h) in a solution of known viscosity (η).[28] Diffusion coefficients calculated based on eq 4 are shown in Table SI2 and compared favorably with the values recovered by FT-FRAP analysis. Viscosities of glycerol/water mixtures were estimated based on temperature and volume fractions of

https://doi.org/10.1021/acs.analchem.3c05728
Anal. Chem. 2024, 96, 10161−10169

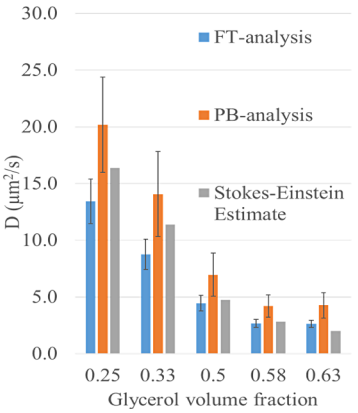

Figure 5. Results are shown for high-throughput analysis of rhodamine-labeled IgG in glycerol/PBS solutions of varying viscosity. Each measurement was performed in ∼2.5 min in 450−600 nL samples prepared robotically in 96-well plates. Error bars indicate one standard deviation across multiple independently prepared droplets, and therefore, implicitly includes both measurement and sample-to-sample variance. Point-bleach (PB) analysis shown in orange systematically recovered faster diffusion coefficients than FT-domain analysis. Theoretical calculations using the Stokes−Einstein equation with estimates for matrix viscosity and hydrodynamic radius of IgG.

glycerol and are shown in Table SI2.[28,29] The hydrodynamic radius of IgG was estimated based on molecular weight (240 kDa) to be ∼5.5 nm.

$$D = \frac{K_b T}{6\pi\eta R_h} \tag{4}$$

Measurement Bias. Relative to FT-FRAP measurements, point-bleach analysis was shown to recover slightly higher diffusion coefficients at all viscosities and exhibit larger experimental uncertainties. Several explanations for the apparent bias between point-bleach and FT-domain analysis were considered.

Deviations from a Gaussian bleach profile will occur at high bleach depths, potentially influencing fits to the initial point-bleach width. In theory, strong photobleaching can result in "top-hat" spatial profiles that deviate substantially from the assumed Gaussian profile used in the fitting. Measurements of the "zero-order" nondiffracted photobleach spot of highest bleach depth revealed point-spread functions inconsistent with a symmetrical 2D Gaussian function. To quantify the role of deviation from a Gaussian PSF on the recovered diffusivity, simulations of stretched Gaussian and top-hat bleach profiles were performed and shown in Figure SI5. For both cases, no significant deviation from the expected recovery in FT-analysis or point-bleach analysis was observed, excluding the role of deviations in PSF as a likely cause for the disparity in recovered diffusion coefficients. Qualitatively similar trends were observed in point-bleach and FT-domain analysis of defocused measurements from atypically broad photobleach PSFs, suggesting against defocusing as a significant source of bias (SI4).

Next, for point-bleach FRAP, deviations from simple exponential decay have been reported previously due to saturation of excited singlet state under high-laser intensities with corresponding optically induced transparency.[18,29] Additional higher-order photophysical processes, including intersystem crossing and excited state absorption, may compete with molecular diffusion as a recovery mechanism, complicating the analysis of the point bleach. If the relaxation times of trapped dark states approach the diffusion recovery time, such processes could significantly perturb the recovery kinetics. FT-FRAP minimizes these collective effects by spreading laser power throughout the sample. Point-bleach fitting to the zero-order bleach spot and a diffracted bleach spot adjacent to the zero-order (SI6) recover a higher D at the zero-order compared to the diffracted spot. Higher laser power at the zero-order could lead to higher-order bleaching kinetics and biasing zero-order point-bleach fitting toward higher diffusivity.

Lastly, the effect of heat deposited during photobleaching was investigated as a potential contributor of bias through photothermal changes in fluorescence quantum yield. As temperature increases, fluorescent quantum efficiency has been shown to generally decrease.[30−32] As thermal diffusion is much faster than molecular diffusion, local gradients in temperature are likely to distribute rapidly across the FoV, then slowly dissipate into the surrounding medium over the larger length scales of the entire FoV. As such, heat deposited during photobleaching may result in a rapid decrease in average fluorescence intensity, recovering as heat dissipates into the semi-infinite surrounding bath. If present, the net effect of this transient reduction and recovery in quantum yield would be a short-term gain in amplitude across all the harmonics with the time-scale of the thermal dissipation into the surrounding bath, with such transient effects most obvious in the lower harmonics that vary over longer time scales. To account for such effects, eq 2 was adapted to include a thermal diffusion term for fitting, yielding a modified recovery function given by eq 5, in which k_{Th} is the thermal relaxation coefficient. Figure SI6 shows representative recovery curves for fits using eqs 2 and 5. In most instances, the amplitude of the thermal contribution (A_{Th}) was low enough to be neglected. From the subset of measurements yielding a significant correction, a thermal decay coefficient of k_{Th}= 0.144 ± 0.009 s^{-1} was recovered in addition to the molecular diffusion coefficient. For a thermal diffusion coefficient of 0.143 mm^2/s, this decay coefficient corresponds to a thermal plume with a root mean squared σ deviation of ∼1.0 mm, which is in good agreement with the FoV size of 1.1 mm × 1.3 mm. If unaccounted, the observed effect from thermal diffusion may cause an underestimation of the recovered diffusion coefficient from the bias in the first few seconds of the recovery curve, with effects more pronounced for faster diffusion species. The effect of sample heating on short-time recoveries (∼8 s) may explain the bias between FT-analysis and point bleach as the heating effect is only observed and straight forwardly decoupled from normal diffusion with FT-domain analysis. The reported values shown in Figure 5 have been corrected for perturbations from thermal bias, with uncorrected values summarized in the Supporting Information.

$$f_{h,k}(t) = A_D\, e^{-(4\pi(h^2+k^2)v_0^2 Dt)}[1 - A_{Th}\, e^{-k_{Th}t}] \tag{5}$$

Diffusion Mapping in Heterogeneous Samples. In addition to the signal-to-noise ratio advantages of FT-FRAP, periodically patterned photobleaching also supports the recovery of spatially resolved diffusion maps. Domains of arbitrary shape can be isolated by image segmentation, with each segmented region independently analyzed for diffusion. Precise image registry using a focal plane array detector has the additional advantage of potentially supporting diffusion analysis in domains with small feature sizes, which is

https://doi.org/10.1021/acs.analchem.3c05728
Anal. Chem. 2024, 96, 10161−10169

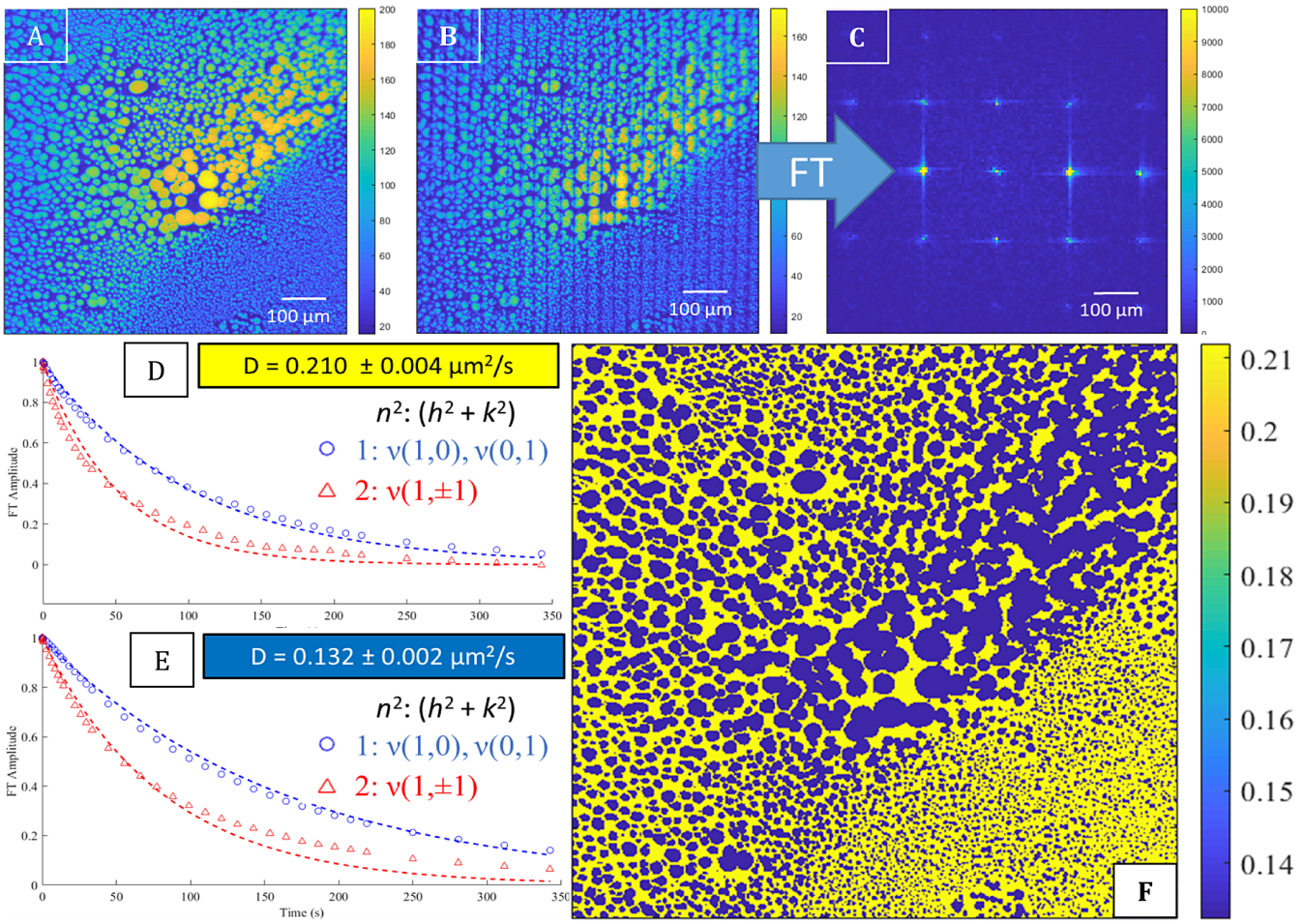

Figure 6. Spatially resolved diffusion analysis in spin-cast films of 15% ibuprofen in PVPVA, using Nile red as a fluorescent reporter. The prebleach image shown in panel (A) shows distinct bright API- dominant regions and polymer-dominant dark regions. The first postbleach image is shown in B. Spatial FT of (B) shown in (C). Colorbars in (A,B) indicate fluorescence intensity recorded as an 8 bit value. Colorbar in (C) indicates integrated intensity from the full image. Recovery curves for segmented domains are shown in panel (D) for fast polymer-dominant recovery, and (E) for API-dominant slower recovery. Image segmentation allows spatially resolved diffusion coefficient recovery ($\mu m^2/s$) (F) in segmented domains of arbitrary shape by FT-FRAP. Colorbar in (F) indicates diffusion coefficient ($\mu m^2/s$) Recoveries recorded at multiple (h,k) spatial FT peaks are consistent with normal diffusion in each domain, with diffusion coefficients differing by nearly 100%.

challenging using previous beam-scanning approaches for FT-FRAP.

Experiments were performed to assess the compatibility of the dot-array pattern produced by diffractive optical elements for spatially resolved diffusion mapping. Representative results are shown in Figure 6 for thin spin-cast films of ibuprofen in a PVPVA polymer matrix. Following exposure to saturated water vapor at elevated temperatures, the spin-cast film spontaneously phase separate into drug-rich and polymer-rich domains. Local viscosity is expected to differ substantially between each of the phase-separated domains, given their differences in chemical composition. In contrast to point-bleach measurements, FT-FRAP has the potential to enable collective analysis across the entire field of view within each of these phase-separated domains in a single experiment. Following phase- separation, identical equilibrium composition is expected within all domains of a given phase. As such, the minimum domain size for diffusion analysis is dictated primarily by image segmentation constraints rather than the highest spatial frequency in the PSF (i.e., the spatial resolution directly accessible by FT-FRAP). In this case, segmentation illustrated in Figure 5 allowed diffusion mapping with domain sizes as small as a few micrometers in cross-section.

Segmented analysis of the drug-rich and polymer-rich domains revealed substantial differences in local diffusivity, with drug-rich domains exhibiting brighter fluorescence and much slower diffusion for the Nile red local reporter, with the two diffusion coefficients differing by approximately 100%. The observation of slower molecular diffusivity within drug-rich phase- separated domains is in good agreement with trends from prior reports in API+PVPVA thin films following water vapor exposure.[23] These results are quite remarkable given the small size of the individual domains within each segmented region. Some domains were only a few micrometers in diameter and comparable in dimension to that of the point-spread function.

In addition to enabling the recovery of domain-specific diffusion coefficients, the FT-FRAP approach also supports the sensitive determination of subtle deviations from normal diffusivity. Consistent with the results for R6G in PVPVA and rhodamine-labeled IgG in aqueous glycerol solutions, the measurements of Nile red in ibuprofen/PVPVA thin films were well described by global fits of multiple (h,k) harmonics with a

https://doi.org/10.1021/acs.analchem.3c05728
Anal. Chem. 2024, 96, 10161−10169

normal diffusion model. These observations are in contrast to prior FT-FRAP studies of ritonavir in PVPVA, following water vapor exposure, in which substantial contributions from interfacial exchange were recorded.[23] The differences are tentatively attributed to differences in glass transition temperatures, T_g, for the two active pharmaceutical ingredients. Whereas T_g is well below ambient temperatures of 20 °C for ibuprofen (−42 °C), it is substantially above for ritonavir (50 °C).[33,34] For ambient temperatures greater than the glass transition temperature, the persistence length of order is reduced, consistent with the observation of normal diffusion.

While the samples investigated herein were intentionally limited to systems exhibiting both normal and isotropic diffusion, the dot-array pattern has the potential to be particularly well suited for the sensitive determination of anisotropies in diffusivity. In lamellar and fibrillar structures, one can reasonably expect significant differences in molecular diffusivity coparallel vs perpendicular to the unique axis in the local frame. If projections of these axes within the FoV align along the primary coordinates of the 2D lattice, differences in decay rates for the (1,0) vs (0,1) peaks in the FT-domain and their corresponding harmonics directly inform the orientation-dependent diffusivity. In the more general case, integration of the decay rates recovered from the complete set of reflections in the FT-domain can be used to recover the three nonzero unique elements of the diffusion tensor D_{xx}, $D_{xy} = D_{yx}$, and D_{yy}. The diagonalization of the diffusion tensor will yield the two principal moments (eigenvalues) and their corresponding directions (eigenvectors) within the FoV. To assess the utility of patterned illumination to probe anisotropic mobility, diffusion coefficients were independently performed along different directions within glycerol/water solutions, the results of which are summarized in the Figure SI4. In such samples, no anisotropies are anticipated; consistent with this expectation, no statistically significant deviations were observed for Miller index sets in different spatial directions [e.g., (1,0) vs (0,1)].

Finally, it is worth commenting on the potential ease with which existing fluorescence microscopes could be retrofitted for FT-FRAP measurements using periodically structured illumination for photobleaching. In beam-scanning confocal microscopes, we have shown previously that integration of FT-FRAP with comb-bleach illumination simply requires software/firmware updates to the slow-scan mirror used to direct the beam across the FoV during the imaging and photobleaching stages, with no required changes to the physical hardware at all.[23] In this work, relatively minor retrofitting of a commercial wide-field microscope with a focal plane array detector was performed by a relatively straightforward addition of the DOE to the beam path and an upgrade to the photobleach laser source. These two microscope designs (confocal beam-scanning and wide field detection with a focal plane array) collectively comprise the overwhelming bulk of systems routinely used for fluorescence microscopy, and correspondingly, for FRAP analysis.

Limitations. The use of FT-FRAP with diffractive optical elements for diffusion mapping, as described herein, has limitations worthy of note. First, as with all FRAP-based methods, FT-FRAP selectively probes the mobility of the fluorophore, which may not be representative of the analyte of interest. For proteins, the addition of a fluorescent label has the potential to change the charge state of the protein, influencing protein−protein and protein−matrix interactions, driving molecular mobility. While two-photon excitation has the potential to enable FT-FRAP using native autofluorescence, the DOE-based architecture is incompatible with multiphoton excitation by distributing intensity across the field of view. For drug/polymer mixtures, the mobility of a fluorescent probe will generally not be identical to the mobility of the API. Native autofluorescence can be achieved by two-photon excitation or UV illumination, but neither is inherently compatible with the use of diffractive optical elements.

CONCLUSIONS

Periodically patterned photobleaching was performed using DOEs and was shown to support automated, high-throughput FT-FRAP of biologically relevant media using a wide-field microscope with a focal plane array detector. Relative to point-bleach FRAP, FT-FRAP with structured illumination reduces sensitivity to the optical PSF, increases the integrated photobleach power, and greatly simplifies the mathematical analysis of diffusion. Furthermore, FT-FRAP with a 2D dot-array pattern was shown to enable the quantification of diffusion at multiple length scales and spatial directions simultaneously. Following a proof-of-concept demonstration, FT-FRAP was used to probe the systematic variability in mouse IgG mobility within media of varying viscosity in high-throughput measurements and phase-separated domains in ibuprofen/PVPVA thin spin-cast films. Potential future applications of FT-FRAP with a DOE for structured illumination during photobleaching include high-throughput analysis of protein mobility within diverse matrices to support structural biology pipelines and for screening protein/excipient and protein/ligand interactions. The ease of retrofitting into existing fluorescence microscopes may also prove advantageous in mapping spatial variations in molecular mobility within biological tissues and *in vivo*.

ASSOCIATED CONTENT

Supporting Information

The Supporting Information is available free of charge at https://pubs.acs.org/doi/10.1021/acs.analchem.3c05728.

FT-FRAP recovery of equidistant harmonics to investigate diffusion anisotropy; influence of defocusing on recovered diffusivity; influence of deviations from photobleach profile on recovered diffusivity; comparison of point-bleach analysis on "zero-order" photobleach spot and adjacent diffracted photobleach spot; influence of photothermal relaxation on recovered diffusivity; theoretical calculations of diffusivity for IgG in various glycerol water mixtures; error analysis for diffusion and photothermal fitting of IgG in glycerol water mixtures (PDF)

AUTHOR INFORMATION

Corresponding Author

Garth J. Simpson − *Department of Chemistry, Purdue University, West Lafayette, Indiana 47907, United States;* orcid.org/0000-0002-3932-848X; Email: gsimpson@purdue.edu

Authors

Dustin M. Harmon − *Department of Chemistry, Purdue University, West Lafayette, Indiana 47907, United States*

Ziyi Cao − *Department of Chemistry, Purdue University, West Lafayette, Indiana 47907, United States;* orcid.org/0000-0002-7461-2902

Alex M. Sherman − *Department of Chemistry, Purdue University, West Lafayette, Indiana 47907, United States*
Nita Takanti − *Department of Chemistry, Purdue University, West Lafayette, Indiana 47907, United States*
Kevin Murati − *Department of Chemistry, Purdue University, West Lafayette, Indiana 47907, United States*
Maura M. Wimsatt − *Department of Chemistry, Purdue University, West Lafayette, Indiana 47907, United States*
Michelle L. Cousineau − *Department of Industrial and Molecular Pharmaceutics, Purdue University, West Lafayette, Indiana 47907, United States*
Yechan Hwang − *Department of Chemistry, Purdue University, West Lafayette, Indiana 47907, United States*
Lynne S. Taylor − *Department of Industrial and Molecular Pharmaceutics, Purdue University, West Lafayette, Indiana 47907, United States;* orcid.org/0000-0002-4568-6021

Complete contact information is available at: https://pubs.acs.org/10.1021/acs.analchem.3c05728

Author Contributions

The manuscript was written through contributions of all authors. All authors have given approval to the final version of the manuscript.

Notes

The authors declare no competing financial interest.

■ ACKNOWLEDGMENTS

The authors gratefully acknowledge funding for the present work from Eli Lilly & Company and from the National Science Foundation (CHE-2004046 and CHE-2305178) and from the NSF Center for Bioanalytic Metrology (IIP-1916691).

■ REFERENCES

(1) Lorén, N.; Hagman, J.; Jonasson, J. K.; Deschout, H.; Bernin, D.; Cella-Zanacchi, F.; Diaspro, A.; Mcnally, J. G.; Ameloot, M.; Smisdom, N.; Nydén, M.; Hermansson, A.-M.; Rudemo, M.; Braeckmans, K. *Q. Rev. Biophys.* **2015**, *48*, 323−387.
(2) Reits, E. A. J.; Neefjes, J. J. *Nat. Cell Biol.* **2001**, *3* (6), E145−E147.
(3) Beaudouin, J.; Mommer, M. S.; Bock, H. G.; Eils, R. *Contrib. Math. Comput. Sci.* **2013**, *4*, 157−169.
(4) Peters, R.; Peters, J.; Tews, K. H.; Bähr, W. *Biochim. Biophys. Acta, Biomembr.* **1974**, *367* (3), 282−294.
(5) Babinchak, W. M.; Surewicz, W. K. *Bio-Protoc.* **2020**, *10* (2), No. e4389.
(6) Offeddu, G. S.; Mohee, L.; Cameron, R. E. *J. Mater. Sci.: Mater. Med.* **2020**, *31* (5), 1−11.
(7) Hashlamoun, K.; Abusara, Z.; Ramírez-Torres, A.; Grillo, A.; Herzog, W.; Federico, S. *Biomech. Model. Mechanobiol.* **2020**, *19* (6), 2397−2412.
(8) Cherezov, V.; Liu, J.; Griffith, M.; Hanson, M. A.; Stevens, R. C. *Cryst. Growth Des.* **2008**, *8* (12), 4307−4315.
(9) Verheyen, E.; van der Wal, S.; Deschout, H.; Braeckmans, K.; de Smedt, S.; Barendregt, A.; Hennink, W. E.; van Nostrum, C. F. *J. Controlled Release* **2011**, *156* (3), 329−336.
(10) Branco, M. C.; Pochan, D. J.; Wagner, N. J.; Schneider, J. P. *Biomaterials* **2009**, *30* (7), 1339−1347.
(11) Kosto, K. B.; Deen, W. M. *AichE J.* **2004**, *50* (11), 2648−2658.
(12) Alvarez-Manceñido, F.; Braeckmans, K.; de Smedt, S. C.; Demeester, J.; Landin, M.; Martínez-Pacheco, R. *Int. J. Pharm.* **2006**, *316* (1−2), 37−46.
(13) Richbourg, N. R.; Peppas, N. A. *Macromolecules* **2021**, *54* (22), 10477−10486.
(14) Richbourg, N. R.; Peppas, N. A. *J. Mater. Chem. B* **2023**, *11* (2), 377−388.
(15) Remaut, K.; Sanders, N. N.; De Geest, B. G.; Braeckmans, K.; Demeester, J.; De Smedt, S. C. *Mater. Sci. Eng., R* **2007**, *58* (3−5), 117−161.
(16) Peeters, L.; Sanders, N. N.; Braeckmans, K.; Boussery, K.; Van De Voorde, J.; De Smedt, S. C.; Demeester, J. *Invest. Ophthalmol. Visual Sci.* **2005**, *46* (10), 3553−3561.
(17) Toseland, C. P. *J. Chem. Biol.* **2013**, *6* (3), 85−95.
(18) Braeckmans, K.; Stubbe, B. G.; Remaut, K.; Demeester, J.; De Smedt, S. C. *J. Biomed. Opt.* **2006**, *11* (4), 044013.
(19) Daddysman, M. K.; Fecko, C. J. *J. Phys. Chem. B* **2013**, *117* (5), 1241−1251.
(20) Hobson, C. M.; O'Brien, E. T.; Falvo, M. R.; Superfine, R. *Biophys. J.* **2020**, *119* (3), 514−524.
(21) Geiger, A. C.; Smith, C. J.; Simpson, G. J. *Multiphoton Microscopy in the Biomedical Sciences XX SPIE* **2020**, *11244*, 123−127.
(22) Geiger, A. C.; Smith, C. J.; Takanti, N.; Harmon, D. M.; Carlsen, M. S.; Simpson, G. J. *Biophys. J.* **2020**, *119* (4), 737−748.
(23) Cao, Z.; Harmon, D. M.; Yang, R.; Razumtcev, A.; Li, M.; Carlsen, M. S.; Geiger, A. C.; Zemlyanov, D.; Sherman, A. M.; Takanti, N.; Rong, J.; Hwang, Y.; Taylor, L. S.; Simpson, G. J. *Anal. Chem.* **2023**, *95*, 2192−2202.
(24) Sun, S.; Zhang, X.; Cui, J.; Liang, S. *Nanoscale* **2020**, *12*, 16657.
(25) Sarkar, S.; Song, Z.; Griffin, S. R.; Takanti, N.; Vogt, A. D.; Ruggles, A.; Danzer, G. D.; Simpson, G. J. *Mol. Pharm.* **2020**, *17*, 769−776.
(26) Fenalti, G.; Abola, E. E.; Wang, C.; Wu, B.; Cherezov, V. *Methods Enzymol.* **2015**, *557*, 417−437.
(27) Wang, X. D.; Wolfbeis, O. S.; Meier, R. J. *Chem. Soc. Rev.* **2013**, *42* (19), 7834−7869.
(28) Edward, J. T. *J. Chem. Educ.* **1970**, *47* (4), 261−270.
(29) Rudemo, M.; Lorén, N.; Jonasson, J.; Hagman, J.; Deschout, H.; Fransson, S.; Braeckmans, K. *Opt. Express* **2010**, *18* (22), 22886−22905.
(30) Li, M.; Razumtcev, A.; Yang, R.; Liu, Y.; Rong, J.; Geiger, A. C.; Blanchard, R.; Pfluegl, C.; Taylor, L. S.; Simpson, G. J. *J. Am. Chem. Soc.* **2021**, *143* (29), 10809−10815.
(31) Chen, T.; Dave, K.; Gruebele, M. *FEBS Lett.* **2018**, *592* (8), 1357−1365.
(32) Gelman, H.; Wirth, A. J.; Gruebele, M. *Biochemistry* **2016**, *55* (13), 1968−1976.
(33) Krummnow, A.; Danzer, A.; Voges, K.; Dohrn, S.; Kyerematen, S. O.; Degenhardt, M.; Sadowski, G. *Pharmaceutics* **2022**, *14* (9), 1904.
(34) Grzybowska, K.; Grzybowski, A.; Knapik-Kowalczuk, J.; Chmiel, K.; Woyna-Orlewicz, K.; Szafraniec-Szczęsny, J.; Antosik-Rogo, A.; Jachowicz, R.; Kowalska-Szojda, K.; Lodowski, P.; Paluch, M. *Mol. Pharma.* **2020**, *17*, 3087−3105.